JOURNAL OF SYNCHROTRON RADIATION
ISSN 1600-5775

Two-dimensional Wide-Angle X-ray Scattering on a Cm-doped borosilicate glass in a beryllium container

Olivier Bouty,[a]* Laure Ramond,[a] Kathy Dardenne[b] and Jörg Rothe[b]

[a]Commissariat à l'Energie Atomique (CEA), Site de Marcoule, DES, ISEC, DE2D, Université Montpellier, BP 17171, 30207 Bagnols sur Cèze, France, and [b]Institute for Nuclear Waste Disposal (INE), Karlsruhe Institute of Technology (KIT), Hermann-von-Helmholtz-Platz 1, 76344 Eggenstein-Leopoldshafen, Germany.
*Correspondence e-mail: olivier.bouty@cea.fr

Received 3 June 2020
Accepted 16 November 2020

Edited by Y. Amemiya, University of Tokyo, Japan

Keywords: wide-angle X-ray scattering; borosilicate glasses; image plates; structure factors; WAXS.

The two-dimensional wide-angle X-ray diffraction technique was applied to a Cm-doped borosilicate glass in a beryllium container. The experiment involved a high-energy X-ray beam and an image plate. It is shown that it is possible to extract the structure factor of the radioactive glass successfully from diffraction patterns and compare it with that of the pristine one. Striking differences appear under the first diffraction peak, revealing new sub-structures for the radioactive glass. It is suggested that they could be related to structural changes in the medium-range order, in particular the size distribution of rings or chains under the influence of mixed interactions between the glass network, α-particles and recoil nuclei.

1. Introduction

Wide-angle X-ray scattering (WAXS) is a relevant technique to gain insight into the structural features of amorphous samples. By assessing the inverse Fourier transform of the interference function or structure factor recorded in reciprocal space, it is possible to extract the total radial distribution function, which allows the main interatomic distances and angles between atomic pairs in the network to be investigated. On the other hand, the structure factor is always an efficient criterion to decide whether or not molecular dynamics simulations are accurate enough to validate the simulated atomistic model. Reliable experimental data also relate to the range of the momentum transfer Q (defined as the modulus of the difference between diffracted and incident wavevectors) which should be as large as possible, to improve the resolution of the Fourier transform and reduce the extent of truncation oscillations. This means that a high-energy beam and/or a large range of diffraction angles is the preferred configuration when preparing an X-ray diffraction (XRD) experiment. As a result, use of X-ray synchrotron radiation is the preferred option.

In the case of samples which undergo extreme conditions (like high temperatures or pressures) or contain radionuclides, several conditions must be fulfilled to comply with the safety rules governing synchrotron beamlines. Therefore, special devices must be designed to ensure the safest experimental requirements. In particular, in the context of a better characterization of alpha self-irradiation effects of incorporated nuclear waste in glass matrices for long-term disposal, there are challenging conditions involved in handling highly radioactive samples: first, reducing the sample volume as much as possible, in order to limit its total activity and lower its

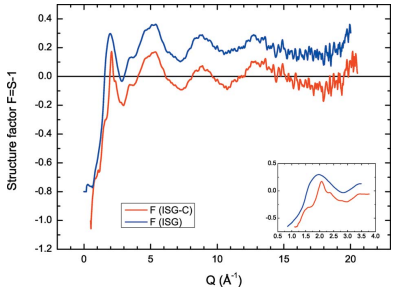

Table 1
ISG and ISG-C glass compositions in wt% of the constituent oxides.

t_0 corresponds to the starting point of the ISG-C damage process.

	SiO_2	B_2O_3	CaO	Na_2O	Al_2O_3	ZrO_2	CmO_2	PuO_2
ISG	56.18	17.33	4.98	12.17	6.06	3.28	0	0
ISG-C (t_0 + 10 years)	55.32	17.07	5.01	12.0	6.03	3.26	0.80	0.62

equivalent dose rate, and second, providing at least a double confinement envelope to reduce contamination risks possibly arising from leakage of radioactive powder in the experimental hutch. Moreover, the containment integrity and its perfect sealing must also be guaranteed under irradiation conditions for any period of time required during the experiment. Hence, sample preparation must be different from usual powder diffraction analysis. To comply with this safety policy, the most valuable technique for obtaining reliable experimental data is given by using X-rays in reflection or transmission mode, while choosing a suitable sample-holder material in terms of thickness, X-ray transparency and integrity under neutron or α-particles emitted from the sample.

Several specific sample holders, designed to adhere to the above-mentioned conditions, already exist: a beryllium dome for XRD analysis of air-sensitive materials (Rodriguez *et al.*, 2008), a hermetic sample holder for XRD of radioactive samples or hazardous specimens (Reibenspies & Bhuvanesh, 2009; Ao *et al.*, 2007; Strachan *et al.*, 2003), a hermetic sample holder for radioactive materials to fit laboratory-based diffractometers (Belin *et al.*, 2004) and a sample cell for liquid studies (Paalman & Pings, 1962). All these holders are suitable for in-house reflection XRD experiments of samples in liquid, powder or pellet form.

Unfortunately, in the present case, preparing a perfectly flat glass fragment or pressing a silicate glass powder without a binder in pellet form is a very demanding and time-consuming solution, especially for the investigation of a highly radioactive glass sample at a synchrotron facility. Therefore, regarding sample preparation time constraints and sample holder safety issues, powder XRD experiments in transmission mode using a sample holder in cylindrical geometry give the most appropriate approach. Thin silicate or quartz capillaries (less than 1 mm inner diameter) or Kapton capillaries must be ruled out, as they provide insufficient mechanical strength and/or hazardous chemical behaviour under neutron or α-particle irradiation. In contrast, beryllium metal (Be) is well suited as its physical properties are compatible with X-ray diffraction (a lightweight element with low X-ray absorption cross section and high mechanical strength) and synchrotron facility constraints (*e.g.* as a vacuum window material). But a Be metal container also has its drawbacks, as it produces a characteristic X-ray diffraction pattern (Meredith *et al.*, 1969), which will overlap with the X-ray diffraction pattern of the amorphous sample. It is therefore the purpose of this work to address how a cylindrical Be container filled with a radioactive sample behaves in a WAXS experiment and to what extent the experimental data can be corrected to extract the structure factor which reflects the structural glass features in reciprocal space.

2. Methods

2.1. XRD samples

The main samples characterized were:

(i) A crystalline silicon powder c-Si (NIST SRM 640d) in a quartz capillary of inner diameter 1.2 mm.

(ii) The International Simple Glass (ISG) in a quartz capillary of inner diameter 1.2 mm. ISG is the borosilicate glass standard for studies related to long-term confinement of nuclear waste (Gin *et al.*, 2013).

(iii) The ISG-C glass in a Be container as described in Section 2.2. ISG-C is the same glass as ISG but curium-doped with 0.73 wt.% ^{244}Cm. ^{244}Cm generally decays into ^{240}Pu by emitting an α-particle and has a long half-life of 18 years. Since its melting and quenching, this glass has accumulated a dose rate greater than $8 \times 10^{18}\ \alpha\ g^{-1}$ (corresponding to a radiation damaging process of 10 years), a value that would be achieved after about 4000 years of storage in a repository for industrial nuclear glass.

Compositions for the ISG and ISG-C glasses are reported in Table 1.

2.2. Beryllium device description

Several sets of three Be metal rods with increasing diameters were carefully machined by a supplier in a controlled area to produce various tubes with only one opening. The inner wall of each tube was threaded at the opening to match a threaded cap. The inner diameter of the smallest tube was 1.1 mm, with a wall thickness of 0.3 mm. The first, second and third Be tubes were all machined to fit into one another (each wall thickness was 0.3 mm). The resulting triple containment followed the principle of Russian nesting dolls (Fig. 1). A leakage test was carried out with one inner tube filled with tritiated water. The container with stacked tubes and threaded caps sealed with a spot of Loctite glue was left for several days in a liquid scintillator. A weak signal appeared above the noise only after 20 days, therefore ensuring that the overall device was safe for a several-day experiment in radioactive conditions.

2.3. Radioactive sample preparation

The ISG-C glass used in this study was initially melted in 2007 at the Atalante hot-cell facility (Bouty *et al.*, 2016). A glass fragment was broken into small pieces of approximately

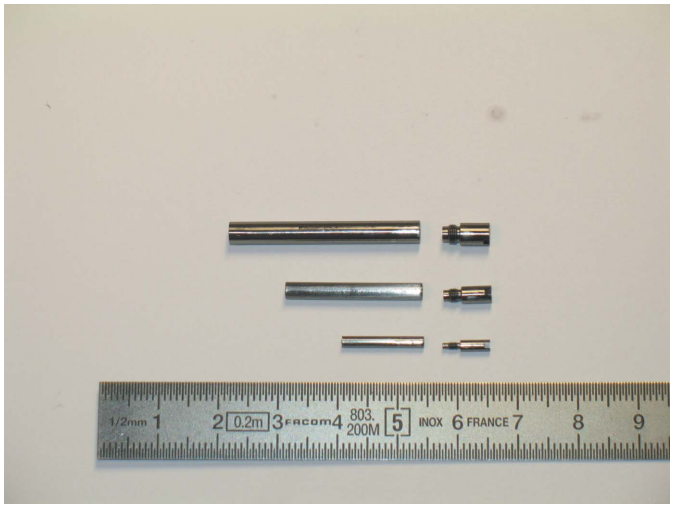

Figure 1
A set of three beryllium tubes with their threaded caps. The final device can be seen as a set of Russian nesting dolls.

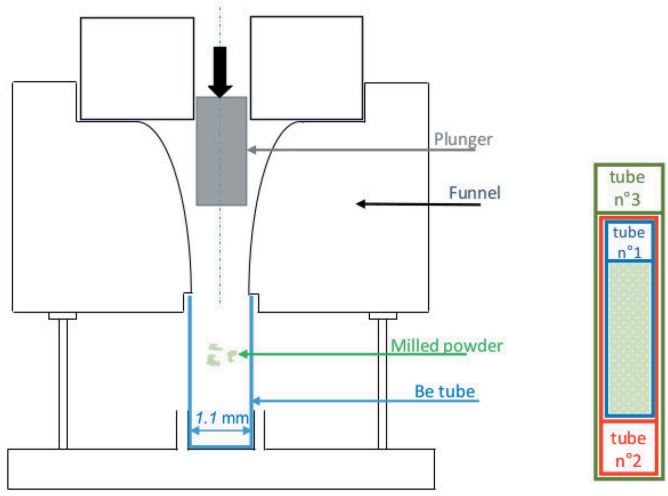

Figure 2
(Left) The setup for introducing the glass powder into the smallest Be tube. (Right) The final device, ready for the X-ray diffraction experiment.

30–35 mg each. One piece was milled in a zirconium oxide grinding jar with two balls in an oscillating ball miller (MM200; Retsch GmbH, Haan, Germany) at 20 Hz for 10 min. A few grains of milled glass (0.3–0.5 mg) were carefully introduced at a time into the funnel (Fig. 2) to avoid spreading glass particles at the top of the inner beryllium tube. At each step, the plunger was depressed to compact the grains efficiently. We managed to fill and compact between 9.7 mg and 9.8 mg of glass powder in the tube, consistent with an average packing factor of at least 0.5. Afterwards, the cap of this tube could be easily screwed on. A spot of glue (Loctite) was also put on the outer thread of the cap to seal the tube. The first operation was carried out in a glove box with a low contamination level in order to limit the surface contamination of the inner Be tube. It was then transferred to a cleaner glove box and placed into the second Be tube like a set of Russian nesting dolls. A dot of glue was again added to the thread of the tube cap to seal it. This assembly was then brought out of the glove box and placed in a fume cupboard, for radiological controls and surface decontamination. The second tube was finally fitted inside the third, outermost, Be tube and its cap sealed with glue.

2.4. The CAT-ACT beamline at KARA

WAXS experiments were performed on the ACT experimental station of the high-flux/high-energy X-ray spectroscopy beamline CAT-ACT (Zimina *et al.*, 2017), operated at the KArlsruhe Research Accelerator (KARA) at KIT Campus North. The beamline comprises two in-line alternately used experimental stations for CATalysis and ACTinide/radionuclide research which share a common optic system receiving photon flux from a superconducting 2.5 T multi-pole wiggler source installed in a 1 m straight section of the KARA storage ring. The CAT-ACT optic comprises a zoned collimating first mirror, a cryo-cooled double-crystal monochromator (DCM) equipped with pairs of Si ⟨111⟩ and Si ⟨311⟩ crystals, and a second mirror with two toroidal sections, providing an elliptically shaped beam spot with dimensions below 1 mm at the two sample positions in the energy range of ∼3.5–35 keV. High-energy operation beyond this limit – as in the present experiment – is performed without mirrors, shaping the beam by four-blade slit systems inside the front end and prior to the sample stage.

2.4.1. WAXS setup on the ACT station. The ACT laboratory is equipped and licensed as a flexible experimental station for X-ray absorption spectroscopy (XAS) and X-ray emission spectroscopy (XES) measurements of radioactive specimens with total activities (sum rule) up to 10^6 times the European exemption limits, including highly radioactive materials like spent nuclear fuel or fragments of original nuclear waste glasses. The experimental equipment comprises, among others, ionization chambers for standard transmission XAS detection mode, solid-state Ge/Si detectors for total yield fluorescence detection and a Johann-type multi-analyser crystal X-ray emission spectrometer for high-energy-resolution X-ray fluorescence detection, enabling high-energy-resolution fluorescence-detected X-ray absorption near-edge structure (HR/HERFD-XANES) and resonant inelastic X-ray scattering (RIXS) measurements.

WAXS patterns of the glass samples were recorded in Laue-type transmission mode using an X-ray sensitive image plate (IP) with a high dynamic range (see next section) as position-sensitive detector. The intensity of the monochromatic beam (I_0) was recorded by an Ar-filled ionization chamber (Poikat, Hamburg, Germany) operated at ambient pressure. The impinging beam was vertically confined by a motorized four-blade high-precision slit (Huber, Rimsting, Germany) with horizontal and vertical gaps of 2000 µm and 500 µm, respectively. The samples – either the Cm-doped glass, the empty container for background measurements or the calibration reference (silicon powder, NIST SRM 640d) in a quartz capillary – were horizontally mounted on top of a high-precision goniometer stage (Huber, Rimsting, Germany). Pre-

alignment was achieved by employing a crossed alignment laser adjusted to the beam height and by moving the beam along a vertical axis crossing the sample while recording the transmitted flux (I_1) with a second ionization chamber or by detecting the Cm $L\alpha$ fluorescence emitted by the sample. For recording the diffraction patterns, the IP was located at a distance of 148 mm or 448 mm (on average) from the sample. The IP was clamped onto a rigid holder bolted to the entrance flange of the second ionization chamber. To collect a larger Q range, the IP holder was positioned off-centre, with the beam axis hitting the lower rim of the films, thus detecting the upper section of the diffraction cone rather than circular fringes. A molybdenum cylinder hung by two horizontally strained nylon threads was used as a central beam stop. A 3 mm lead sheet with a central aperture was positioned immediately downstream of the four-blade slit to prevent diffuse scattering signals from reaching the detector. The image quality was further improved by fixing an additional lead foil on the sample holder immediately above the cylindrical sample containment. No filters were placed in front of the IP to suppress any possible Cm fluorescence contribution. Finally, the accuracy of the diffraction pattern depends on the best compromise between sample and screen distance, wavelength and diffraction angular range. In our experiment, the chosen parameters combined with a vertically mounted IP (24 cm × 12 cm usable area) allowed a maximum momentum transfer (Q value) of 24 Å^{-1} to be reached.

The X-ray beam wavelength was tuned to 0.246 Å by calibrating the DCM to the gadolinium K-edge XANES. A thin Gd metal layer was used to this end in transmission mode (the first inflection point in the absorption spectrum of a Gd_2O_3 sample was assigned to the Gd 1s energy of 50.24 keV). The polarization of the beam is usually defined as $f = (I_\sigma - I_\pi)/(I_\sigma + I_\pi)$, where I_σ and I_π are the vertical and horizontal components of the intensities, respectively. Unfortunately, an exact polarization value could not be measured during the experiment. Therefore, we assumed 98% horizontally polarized radiation on average, with reference to already known values found on other synchrotron beamlines (between 95 and 99%). The distance between the sample and the detector was initially set to 148 mm, but this value was submitted to refinement during the diffraction image integration procedure.

2.4.2. Two-dimensional (2D) image-plate detector on the ACT station. The detection device used was a flexible reusable storage phosphor screen (PerkinElmer Inc., USA). This multi-sensitive IP, coated with a photostimulable phosphor layer based on the alkali-halide compound BaFBr:Eu^{2+}, has a high luminescence efficiency for X-ray excitation (Li *et al.*, 2002; Meadowcroft *et al.*, 2008; Tisseur *et al.*, 2014; Rowlands, 2002; Amemiya *et al.*, 1987). As the IP does not discriminate between different X-ray energies, overlapping X-ray fluorescence radiation emitted by the sample might hamper the analysis of the stored X-ray scattering signals. The IP used during our experiment can be compared with a MAR345 phosphor screen, for which the absorption efficiency was already assessed by Jakoncic *et al.* (2006) for X-ray beams with energy in the range 1–100 keV. In particular, an absorption efficiency of 45% was measured by the authors at almost 50 keV, a value which can be reasonably assumed for our IP system (the published absorption efficiency curve is very similar to the Ba absorption curve with a K edge at 37.4 keV). Several exposure times were tested during the experiments to adapt the irradiation conditions to the dynamic range of the storage material. Data were collected with exposure times up to 300 s. After each X-ray diffraction experiment, the IP was read out by a Cyclone Plus laser scanner (PerkinElmer Inc., https://www.perkinelmer.com/). A digitized high-resolution image containing the stored X-ray intensities for each pixel in greyscale was created at 600 d.p.i. using *OptiQuant*™ software (PerkinElmer Inc.). As the IP dimensions were 12.5 cm × 25 cm, a scan rate of 600 d.p.i. corresponds to a screen containing 2995 × 5806 pixels with a pixel size of 42.33 µm. Before reusing the IP, all stored information was erased by exposing the X-ray sensitive surface to UV light for at least 15 min.

3. Description of correction procedure

The correction procedure can be divided into three steps: a first step with basic image processing, a second step gathering all corrections corresponding to the main physical phenomena like absorption, polarization, fluorescence and geometry, and a last step for data normalization.

3.1. First step: image processing

Amemiya *et al.* (1987) mentioned that the intrinsic microscopic non-uniformity and image distortion for a similar IP was estimated to be of the order of 1%. Therefore, with reference to the IP performance specifications given by the supplier, neither non-uniformity of the detector response nor spatial distortion as described by Hammersley *et al.* (1995) were considered here. In contrast, after readout, the IP erasure process is not 100% efficient as noted by He (2018), leaving a ghost image which must be taken into account when processing the digitized files with the image-processing software. Experimentally, scanned and digitized IPs after the erasure procedure showed that this contribution remained weak and almost the same whatever the experimental conditions were. Moreover, a top-hat smoothing of 25 × 25 was applied on all images. Noise and high spatial frequencies are therefore significantly reduced.

3.2. Second step: main corrections

Extending the notations of Skinner *et al.* (2012), a basic correction formula for the experimental intensity can be written as

$$I_S(\theta) = \left\{ \left[I_{SCB}(\theta) - I_{SCB}^{MS}(\theta) - I_{SCB}^{FL}(\theta) \right] \frac{T_S}{A_S(\theta)} - I_{CB}(\theta) \right\} \times \frac{T_C}{A_C(\theta)} \left[\frac{1}{G(\theta)\, P(\theta)\, A_{IP}(\theta)} \right], \quad (1)$$

where 2θ is the diffraction angle, I_{SCB} is the measured intensity from the sample + container + background, I_{CB} is the

diffracted intensity resulting from the empty container + background, I_{SCB}^{MS} is the multiple scattering intensity and I_{SCB}^{FL} is the fluorescence generated by the irradiated sample and leaving the container. A_C and A_S are the absorption of the container and the sample, respectively, and T_C and T_S are the transmission factors corresponding to diffraction at normal incidence. G, P and A_{IP} are geometric, polarization and incomplete IP absorption factors, which all depend on the diffraction angle 2θ.

The X-ray fluorescence contribution results from the de-excitation of an atom after being irradiated by high-energy X-rays beyond its ionization potential relative to a core electron. Fluorescence emission due to core–shell excitation may come along with the emission of Auger or photo-electrons from shallower electronic levels during the de-excitation cascade. Fluorescence photons are characteristic of an element and are the basis for material elemental analysis. By means of quantum physics methods, several models describe the directional distribution of emitted photo-electrons depending on their energy and polarization (Basaglia *et al.*, 2013; Hemmers *et al.*, 1997; Trzhaskovskaya *et al.*, 2001, 2002). But in contrast, to our knowledge, there are few models to describe fluorescence corrections for X-ray diffraction in the literature. One of the most recent by Soper and Barney is mainly based on the spectrum of incident X-rays relative to *Bremsstrahlung* and photon attenuation in the sample (Soper & Barney, 2011). More generally, there is a lack of quantum models related to X-ray fluorescence phenomena for describing the angular dependence of emitted X-ray fluorescence photons. This issue will be addressed below.

The multiple scattering process cannot be avoided in transmission geometry for thin samples, large diffraction angles and high-energy X-rays (beyond 50 keV), as paths for multiply scattered photons before leaving the sample could be shorter than for singly scattered ones, therefore contributing non-negligibly to the total scattered intensity. To describe this contribution, we will follow the results of the Monte Carlo model developed by Serimaa *et al.* (1990). In particular, they show that for light elements such as Al or C, the multiple scattering contribution increases with Q. This contribution rises linearly with Q for thin samples in transmission geometry for diffraction angles smaller than 60° (see Fig. 1 in their paper). As a generalized model is not available to our knowledge at the moment, we will extrapolate their conclusions to our samples in the same angular range, but for a shorter wavelength. The multiple scattering correction (MS) will therefore be based on the following expression: $I_{SCB}^{MS} = \delta Q I_{SCB}$. The parameter δ is chosen to fit correctly the asymptotic part of the corrected experimental intensity to the combination of both independent elastic and inelastic contributions, as described below. The amplitude of δ is always below 0.1 and depends on the incident X-ray beam's energy. The G term results from the combination of two geometric corrections g and SA:

$$G(\theta) = g(\theta)\, SA(\theta). \tag{2}$$

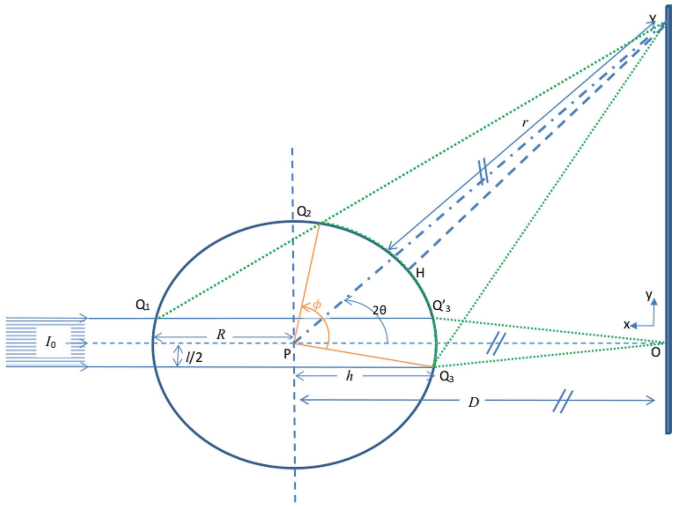

Figure 3
A schematic representation of the set-up and the relative length on the sample seen by a pixel on the IP, depending on the diffraction angle.

The correction g can be seen as the result of the projection of the flat IP onto a spherical surface (in other words assessing the solid angle). It is due to the pixel intensity angular decrease with respect to a rising diffraction angle, normalized by the pixel intensity at the detector origin [see for example He (2018)],

$$g(\theta) = \cos^3(2\theta). \tag{3}$$

The correction SA relates to the recorded intensity by each pixel on a spherical IP which depends on the container's observed surface. This surface relies on the diffraction volume based on the intersection between the X-ray beam and the sample (see Fig. 3). By definition, the intensity received by a pixel is the amount of carried energy per solid angle related to the observed area: $dI = dE/d\Omega$, with $d\Omega = d\mathbf{S} \cdot \mathbf{u}/r^2$, where $d\Omega$ is the solid angle, $d\mathbf{S}$ the observed surface, $\mathbf{u}$ a unitary vector pointing in the direction of observation and r the distance from one pixel to the outer surface of the container in the normal direction. In the case of an infinite cylindrical container in the z direction, the solid-angle expression simplifies to $d\omega = d\mathbf{L} \cdot \mathbf{u}/r$, where $d\mathbf{L}$ is the curvilinear length of one side of the observed area. Therefore, the normalized differential SA correction takes the form

$$d[SA(\theta)] = \frac{d\mathbf{L}(\theta) \cdot \mathbf{u}}{\mathbf{L}_0 \cdot \mathbf{u}_0}, \tag{4}$$

where $\mathbf{L}_0$ corresponds to the curvilinear length seen by a pixel at the axis origin located on the plate and pointing along the container radial axis of symmetry. The SA correction is specific to the chosen experimental setup and its mathematical formalism is presented in Appendix *A*. As an example, Fig. 4 shows how the SA correction correlates with the beam diameter.

The factor P corresponds to the two-dimensional polarization correction (Kahn *et al.*, 1982) derived as

$$P(\theta) = 0.5\left[\left(1 + \cos^2 2\theta\right) - \left(f' \cos 2\varphi \, \sin^2 2\theta\right)\right], \tag{5}$$

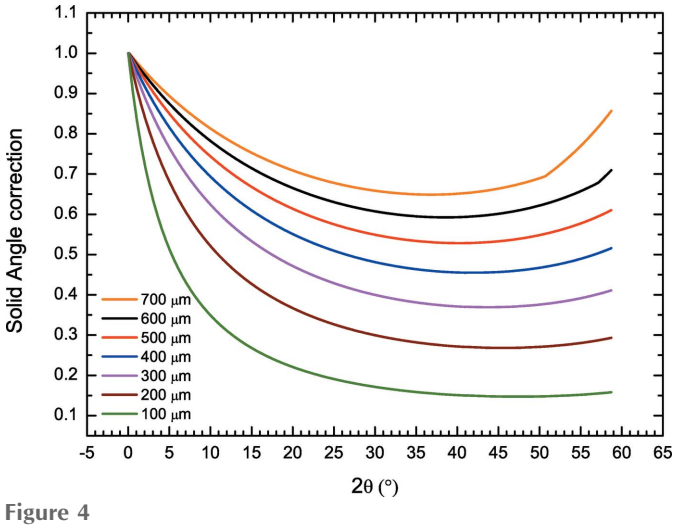

Figure 4
Solid-angle correction versus diffraction angle for different beam diameters in the experimental setup.

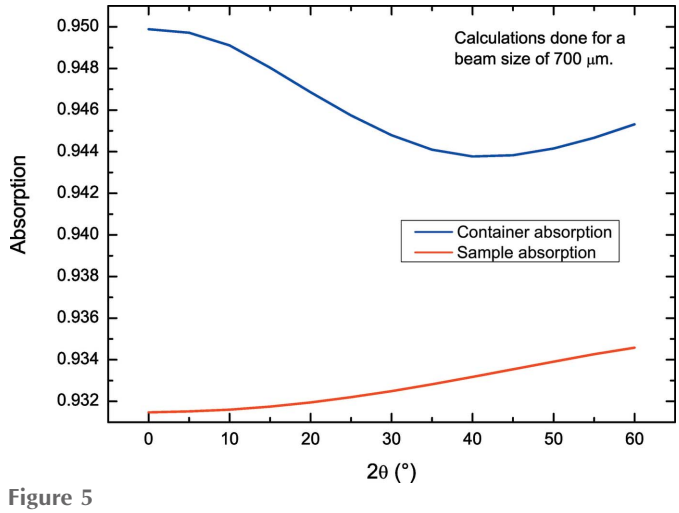

Figure 5
Absorption corrections for ISG glass (blue curve) and the empty Be container (red curve). The curves correspond to a beam of 700 µm diameter.

where 2θ is the diffraction angle, 2φ is the azimuthal angle on the detector plane, and f' is the modified polarization factor combining monochromator crystal and sample contributions. Geometric g and polarization P corrections are usually provided by image-processing software like *FIT2D* (Hammersley, 2004). $A_{\rm IP}$ corresponds to the IP incomplete absorption (Zaleski *et al.*, 1998), which depends on the diffraction angle 2θ, the linear absorption coefficient μ of the layer and its thickness d:

$$A_{\rm IP}(\theta) = \frac{1 - \exp(-\langle \mu d \rangle / \cos 2\theta)}{1 - \exp(-\langle \mu d \rangle)}. \quad (6)$$

As μ is angle-dependent, Compton scattering should also be taken into account and the latter relation corrected. But to avoid a too-lengthy expression and new unknown parameters, we chose to replace μd by an average value $\langle \mu d \rangle$ reflecting the inclusion of Compton effects.

Now, considering data presented by Jakoncic *et al.* (2006), Rowlands *et al.* (2002) and Tisseur *et al.* (2014) for a MAR345 phosphor screen made from BaFBr:Eu^{2+}, the absorption efficiency at normal incidence for 50 keV X-ray photons reaches 0.45. If $T_\perp$ is defined as the transmitted intensity at normal incidence, $\langle \mu d \rangle = {\rm Ln}[1/(1 - T_\perp)] = 0.597$. Therefore, it can be inferred for a 200 µm screen thickness on average that $\langle \mu \rangle = 29.9$ cm^{-1}. Moreover, with a packing factor of 0.5, $\langle \mu \rangle / \rho$ can be estimated to be 10.5 cm^2 g^{-1} at 50.24 keV, which is not far from the value of $\langle \mu \rangle / \rho$ for barium at the same energy.

$A_{\rm S}$ and $A_{\rm C}$ correspond to the absorption from the sample and its container, respectively. They result from X-rays travelling through different materials, and may combine singly and multiply scattered X-rays. As this phenomenon depends on the container and sample geometry, simulating the absorption by means of X-rays which propagate through the sample and the container towards the IP appears to be an accurate solution. In this context, we chose to follow the direct method presented by Damay & Idrissi (2006). In this model, air, sample and container are discretized by squared cells in a large array with different ascribed attenuation coefficients. A beam element enters the array along an axis perpendicular to the IP, moves from one cell to another until scattering occurs in either the container or the sample, and then follows the new direction until it reaches one of the grid borders. The transmission of the beam element is calculated in each cell along its path with the related absorption value. Fig. 5 illustrates the absorption amplitude versus diffraction angle for a typical cylindrical sample.

3.3. Third step: data normalization

Before obtaining the physical quantity of interest referred to as the interference function (or structure factor), we have to express the corrected intensity in terms of atomic units,

$$N I_{\rm exp}^{\rm corr} = I^{\rm cc} + I^{\rm cu} + I^{\rm i}, \quad (7)$$

where $I_{\rm exp}^{\rm corr}$ is the experimental intensity to which apply all previous described corrections, and $I^{\rm cc}$ and $I^{\rm cu}$ are the coherent (or elastic) contributions including the constructive and destructive interference parts and the one from the uncorrelated atomic system. $I^{\rm i}$ is the incoherent (or inelastic) scattering intensity which describes the Compton effect (wavelength shift from the coherent λ scattering to the incoherent λ' scattering), and takes into account the relativistic Klein–Nishina correction derived from quantum physics principles (Das *et al.*, 2014; Klein & Nishina, 1929) and applied to a linearly polarized incoming photon with scattering angle 2θ and azimuthal angle φ,

$$R_{\rm K\text{-}N}(\theta, \varphi) = \left(\frac{\lambda}{\lambda'}\right)^3 \frac{\left[1 + (\lambda'/\lambda)^2 - (\lambda'/\lambda)\, 2 \sin^2 2\theta \cos^2 \varphi\right]}{\left[1 + \cos^2 2\theta \cos^2 \varphi\right]}, \quad (8)$$

or its counterpart approximation, the so-called Breit–Dirac electron recoil factor,

$$R_{\rm B\text{-}D} = \left(\frac{\lambda}{\lambda'}\right)^3 = \left(1 + \frac{2h}{mc^2 \lambda \sin^2 \theta}\right)^{-3}. \quad (9)$$

with an exponent of 3 when intensities are measured by the detector as for IPs (Manninen *et al.*, 1984). N is a normalization factor obtained by the Krogh–Moe method (Krogh-Moe, 1956). I^{cu} and I^{i} are assessed from X-ray form-factor tabulations (Waasmaier & Kirfel, 1995) and Compton coefficients (Balyuzi, 1975): $I^{cu} = \sum_\alpha c_\alpha c_\beta f_\alpha(Q) f_\beta(Q)$ and $I^{i} = C[\sum_\alpha c_\alpha f_\alpha(Q)]^2$, where C relates to the Breit–Dirac or Klein–Nishina correction. In our approach, multiple scattering is not applied to Compton profiles, to avoid too many free parameters during data corrections (Felsteiner *et al.*, 1974). The so-called interference function F or structure factor $S = F + 1$ is afterwards inferred in absolute electron units as (Klug & Alexander, 1974)

$$F(Q) = \frac{I^{cc}}{I^{cu}}(Q) = \frac{NI^{corr}_{exp}(Q) - \left\{\sum_\alpha c_\alpha c_\beta f_\alpha(Q) f_\beta(Q) + \left[\sum_\alpha c_\alpha f_\alpha(Q)\right]^2\right\}}{\left[\sum_\alpha c_\alpha f_\alpha(Q)\right]^2}. \quad (10)$$

4. Results and discussion

The first X-ray diffraction experiment was performed on c-Si as a standard. It mainly enabled us to improve the setup and verify its efficiency in recording X-ray diffraction patterns. Furthermore, helped by *FIT2D*, the sample-to-detector distance, the X and Y coordinates of the direct beam and the detector non-orthogonality (tilt angle) were refined during image calibration, including the polarization and the geometric correction g.

As a second round, we collected the ISG 2D image and used the integrated intensity to correct it from the following contributions: multiple scattering, sample absorption, empty container, container absorption, solid angle and high-angle IP absorption. All the corrections corresponding to the aforementioned contributions were combined to proceed with the normalization procedure of the spectrum (Fig. 6) while using a minimization algorithm to optimize the beam width (related to *SA*) and MS effect. A satisfying structure factor was obtained within the range 0.5 Å^{-1} ≤ Q ≤ 20 Å^{-1} for a beam width of 700 µm and a δ (MS) factor of 5×10^{-3} (Fig. 7). This δ value was later used as a starting point for the ISG-C correction procedure. It is worth noting that, in contrast to what is claimed by some authors, there is no need to use negative exponents (like −20 or −30) for the Breit–Dirac correction, which reverse its physical meaning and make it wrong [see for example Marcial *et al.* (2019)].

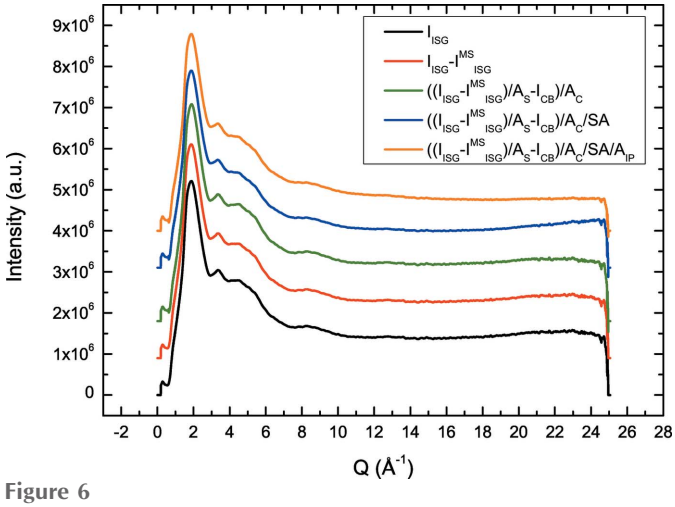

Figure 6
Corrections applied to the ISG intensity integrated pattern. From bottom to top: intensities related to ISG glass, ISG glass − MS, [(ISG glass − MS)/A_S − CB]/A_C, [(ISG glass − MS)/A_S − CB]/A_C/SA and {[(ISG glass − MS)/A_S − CB]/A_C}/SA/A_{IP} [see equation (1) for details]. Polarization and geometric g corrections are taken into account during the *FIT2D* integration procedure. The curves are displaced vertically for clarity.

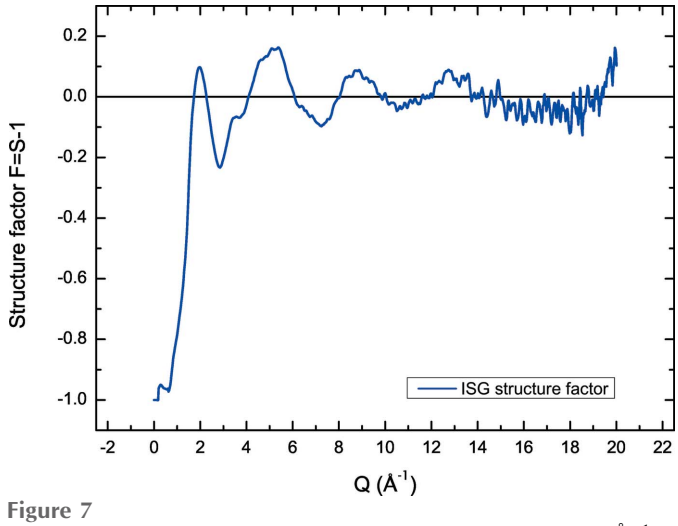

Figure 7
ISG structure factor $F = S - 1$ versus momentum transfer Q (in Å^{-1}).

Afterwards, X-ray diffraction was performed on the radioactive ISG-C glass. In Fig. 8, the ISG-C recorded pattern clearly shows the presence of several contributions: the first one emerging from the glass, the second one coming from the Be metal and the third one related to the strong fluorescence arising from some glass components. This means that even for

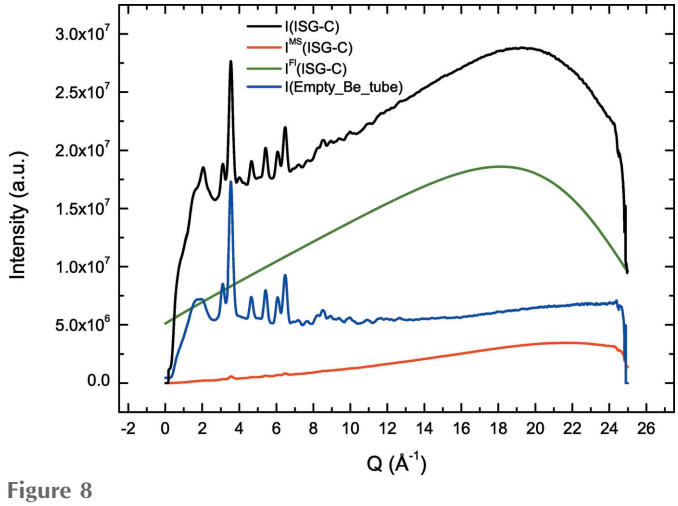

Figure 8
A comparison between the ISG-C intensity integrated pattern (black curve) and the contributions from fluorescence (green curve), the empty Be tube (blue curve) and multiple scattering (red curve).

50 keV incoming X-rays, fluorescence can occur via multiple inelastic processes. The possible elements involved are Zr, Cm and Pu. Zr fluorescence should mainly be significant for the K absorption edge (18 keV), in contrast to Cm and Pu for which it should be significant for L_1, L_2 and L_3 absorption edges (between 18.97 and 24.52 keV for Cm, and 18.06 and 23.10 keV for Pu). Moreover, a description of the photoionization cross section of the L shell as a function of atomic number for an average photon energy of 59 keV (Han *et al.*, 2016; Basaglia *et al.*, 2013) shows a power-law dependence which implies a ratio between Cm and Zr cross sections always greater than 10. It is therefore highly likely that the observed fluorescence originates mainly from Cm, less from Pu and far less from Zr.

Following X-ray atomic databases for X-ray spectroscopy [see for example Elam *et al.* (2002)], Cm fluorescence photons mainly emerge from electronic transitions associated with the L_1 (24.52 keV) and L_2 (23.65 keV) absorption edges, with photons of 19.42 keV corresponding to the most likely transition L_2–M_4. At first glance, it is expected that X-ray fluorescence is isotropically distributed with an intensity proportional to the electronic transition probabilities involved, but there is also no reason that this angular distribution will not correlate more or less with that of photoelectrons.

Therefore, relative to the above remarks on fluorescence, and to avoid too rough an estimate of the Cm X-ray fluorescence contribution from the diffraction experiments, we suggest building a model where the angular distribution of X-ray fluorescence at a given incident photon energy is the combination of an isotropic component and an anisotropic one but correlated to that of the photoelectrons. Following this hypothesis, a linear relation can be inferred between the scattering angle of the fluorescence photon and the angle defined by the ejected photoelectron with the polarization vector of the incident photon. There already exist expressions for differential photoionization cross sections obtained in the dipole approximation, describing the angular dependence of photoelectrons (Hemmers *et al.*, 1997). We will therefore handle our fluorescence model with the following basic expression which reflects a similar behaviour [see for example Fig. 53 in the work of Han *et al.* (2016)]:

$$I_{\rm SCB}^{\rm FL}(Q) = \left[{\rm FL}(0) + \alpha Q^{(1-\beta)}\right] \exp\left[-\left(\frac{Q}{Q_0}\right)^{\gamma}\right], \quad |\beta| \ll 1. \tag{11}$$

The fluorescence first rises sharply, then reaches a maximum and finally falls exponentially for high Q values. All parameters FL(0), α, β, γ and Q_0 were optimized by a minimization procedure for the combination of ISG glass, empty Be tube, sample and Be container absorption and fluorescence contributions to reproduce both the asymptotic part of the ISG-C diffraction pattern and an isotropic contribution when Q approaches 0. The fluorescence intensity is presented in Fig. 8.

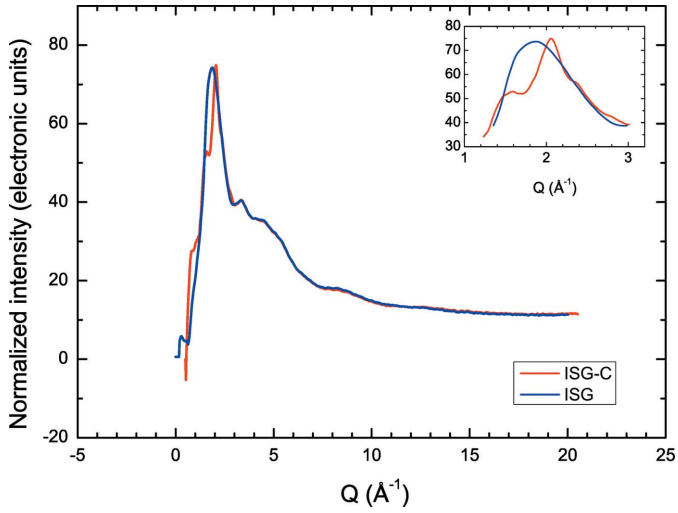

Figure 9
A comparison between the corrected ISG-C and ISG intensity integrated patterns. The intensities are normalized to electronic units. The inset focuses on the different features which can be seen under the first large peak located around 2 Å^{-1}.

Finally, it can also be pointed out that a small Bragg peak appears around 4 Å^{-1} (which can be seen in the ISG-C pattern in Fig. 8), but as a previous XAFS study did not show any crystallization issue (Bouty *et al.*, 2016), it is likely that this peak is either due to ZrO_2 contamination from the grinding jar or from parasitic X-rays reflected by metallic structures surrounding the setup. It was therefore removed from the pattern before starting the correction and normalization procedure. The same strategy as for ISG was applied to the ISG-C intensity integrated pattern, while taking into account the contribution from the empty Be container in addition to the contributions already identified for ISG. As a result, a new structure factor was found in the range 0.5 Å^{-1} $\leq Q \leq$ 20.5 Å^{-1}, with a δ (MS) factor of 5.8×10^{-3}, which could be explained by taking into account a small Be contribution.

The most striking differences between ISG-C and ISG corrected intensities (displayed in Fig. 9 and in the inset) are located in the low-Q region, where new sub-structures clearly appear below the first ISG-C large peak around 2 Å^{-1}. Other small deviations are also present beyond 8 Å^{-1}, but unfortunately cannot be discussed here as the uncertainty over fluorescence and multi-scattering contributions grows with increasing Q values.

Fig. 10 depicts the variations between the structure factors extracted from ISG and ISG-C normalized intensities. While focusing on the low-Q region, it is possible to assert that at least three new sub-structures are present under the so-called first diffraction peak (FSDP). At first sight, the one on the left is centred around 1.6 to 1.7 Å^{-1} and reveals a large intensity drop. The second one is located around 2 to 2.1 Å^{-1} and reflects a small rise in intensity. The third one results in an inflexion point located around 2.4 to 2.5 Å^{-1}.

The FSDP has been widely discussed in the literature since the late 1980s, in particular for chalcogenide and silicate glasses (Elliott, 1995; Wright, 1994), but several issues are still

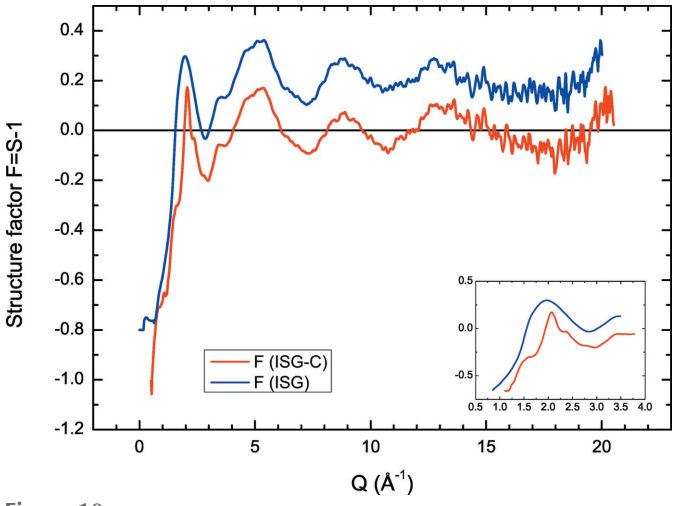

Figure 10
A comparison between the ISG (blue curve) and ISG-C (red curve) structure factors. The inset focuses on the sub-structures appearing under the FSDP. The curves are displaced vertically for clarity.

under discussion to understand better what kind of information relates to this peak. According to the work of Wright, we can expand the FSDP as a combination of several Gaussians, each one located at a special Q_n position. Its reverse Fourier transform results in another Gaussian, but damped by a sine function with a $2\pi/Q_n$ period. Rather than referencing to a 'distance' or a 'period', this value could also be seen as a 'characteristic length' describing 'scattering objects' paving the glass network. Low Q values can therefore be related to large characteristic lengths, describing rings or chains under the influence of mixed interactions between the glass network, α-particles and recoil nuclei. Following this analysis, Table 2 provides in real space the three characteristic lengths determined from the Q values identified under the FSDP.

In the medium-range order, three and four-membered rings are common structures found in borosilicate glasses. Three-membered rings are built upon SiO_4 silicate tetrahedra, and are often referred to as D_2 rings. Moreover, Danburite- and Reedmergnerite-like rings are four-membered rings (Holbrook *et al.*, 2014), incorporating alternately SiO_4 and BO_4 tetrahedra. A rough estimate of the circumcircle diameter ϕ encircling three SiO_4 triangle vertices based on the expression $\phi = 2a/\sqrt{3}$, where a represents an average value for the Si—Si bond length in silicate glasses and is assessed as 3.1 Å, gives a value of 3.6 Å, which is not far from the first characteristic length. The Si—Si distance can also be found in D-like rings and is consistent with the second characteristic length. In contrast, the third value seems to be close to the O—O distance and cannot be related to a ring. We therefore suggest that at least two sub-structures can be associated with three and four-membered rings and their distribution could vary with Gaussian heights. Finally, a more precise study will need to be done by assessing the first and second derivatives of the structure factor below 2 Å^{-1}, locating precisely the inflexion points and extrema, and inferring all the characteristic lengths and related objects which could appear under the FSDP.

Table 2
Characteristic length in real space versus momentum transfer Q.

	Q (Å^{-1})		
	1.6–1.7	2.0–2.1	2.4–2.5
Characteristic length (Å)	3.7–3.9	2.9–3.1	2.5–2.6

5. Conclusions

For the first time, we have managed to apply the 2D wide-angle X-ray scattering technique to a Cm-doped borosilicate glass fitted inside a beryllium container. The experimental setup involved a 50 keV high-energy X-ray beam and an image plate. Even though such a configuration brings some drawbacks, for example a large Cm fluorescence contribution or a crystalline Be contribution which partially blurs the diffraction patterns, we have shown that it is possible to extract successfully the structure factors of both the pristine and Cm-doped glass samples. Striking differences appear under the first diffraction peak, which cannot be ascribed only to already known effects like thermal or compositional dependencies. It is more likely that the new sub-structures are related to changes in the size distributions of large objects like rings or chains under the influence of mixed interactions between the glass network, α-particles and recoil nuclei.

APPENDIX *A*
Mathematical formulas

$$K = \frac{D\tan(2\theta) - l/2}{D + R\cos\alpha}$$

$$A = (1 + K^2)$$

$$B = -2K(l/2 + KD + KR\cos\alpha) - 2D$$

$$C = (l/2 + KD + KR\cos\alpha)^2 + D^2 - R^2$$

$$\Delta = B^2 - 4AC$$

$$x_Q = \frac{-(B + \sqrt{\Delta})}{2A}$$

$$y_Q = \left[R - (x_Q - D)^2\right]^{1/2}$$

$$\alpha = \arcsin(l/2R)$$

$$x_H = D - [R\cos\alpha\cos(\phi/2) + l/2\sin(\phi/2)]$$

$$y_H = [R\cos\alpha\sin(\phi/2) - l/2\cos(\phi/2)]$$

$$\phi = \arccos\{R^{-2}[RD\cos\alpha - (x_Q R\cos\alpha + y_Q\, l/2)]\}$$

$$\delta L = \phi R$$

$$SA(\theta) = \frac{\delta L}{R}\left\{\frac{x_H(D - x_H) - y_H\left[y_H + \tan(2\theta)\right]}{x_H^2 + \left[y_H - D\tan(2\theta)\right]^2}\right\}.$$

Variables refer to equation (4) and are shown in Fig. 3.

Acknowledgements

The authors express particular thanks to P. Coste, E. Mendes, J. Delrieu and S. Lemius from CEA Marcoule for technical and logistic support during sample preparation, and J. M. Vacher from VCN Industries (France) for machining the Be rods. We gratefully acknowledge the KIT light source for provision of beam time in the ACT laboratory operated by the Institute for Nuclear Waste Disposal (INE) and would like to thank the Institute for Beam Physics and Technology (IBPT) for operation of the Karlsruhe Research Accelerator (KARA) storage ring.

References

Amemiya, Y., Kamiya, N., Satow, Y., Matsushita, T., Chikawa, J., Wakabayashi, K., Tanaka, H. & Miyahara, J. (1987). *Biophysics and Synchrotron Radiation*. *Springer Series in Biophysics*, Vol. 2, edited by A. Bianconi & A. Congiu Castellano, pp. 61–72. Heidelberg: Springer.

Ao, B., Wang, X., Wei, Y. & Zhang, Y. (2007). *J. Appl. Cryst.* **40**, 796–798.

Balyuzi, H. H. M. (1975). *Acta Cryst.* A**31**, 600–602.

Basaglia, T., Batic, M., Han, M. C., Hoff, G., Kim, C. H., Kim, H. S., Pia, M. G. & Saracco, P. (2013). *arXiv*:13115153 Phys.

Belin, R. C., Valenza, P. J., Reynaud, M. A. & Raison, P. E. (2004). *J. Appl. Cryst.* **37**, 1034–1037.

Bouty, O., Ramond, L., Solari, P. L. & Cammelli, S. (2016). *J. Mater. Sci.* **51**, 7918–7928.

Damay, P. & Idrissi, A. (2006). *Physica B*, **382**, 71–75.

Das, G., Tiwari, M. K., Singh, A. K. & Ghosh, H. (2014). *J. Anal. At. Spectrom.* **29**, 2405–2413.

Elam, W. T., Ravel, B. D. & Sieber, J. R. (2002). *Radiat. Phys. Chem.* **63**, 121–128.

Elliott, S. R. (1995). *J. Non-Cryst. Solids*, **182**, 40–48.

Felsteiner, J., Pattison, P. & Cooper, M. (1974). *Philos. Mag.* **30**, 537–548.

Gin, S., Abdelouas, A., Criscenti, L. J., Ebert, W. L., Ferrand, K., Geisler, T., Harrison, M. T., Inagaki, Y., Mitsui, S., Mueller, K. T., Marra, J. C., Pantano, C. G., Pierce, E. M., Ryan, J. V., Schofield, J. M., Steefel, C. I. & Vienna, J. D. (2013). *Mater. Today*, **16**, 243–248.

Hammersley, A. P. (2004). *FIT2D Reference Manual Version 6.0*. Report 98HA01T. European Synchrotron Radiation Facility, Grenoble, France.

Hammersley, A. P., Svensson, S. O., Thompson, A., Graafsma, H., Kvick, A. & Moy, J. P. (1995). *Rev. Sci. Instrum.* **66**, 2729–2733.

Han, M. C., Kim, H. S., Pia, M. G., Basaglia, T., Batič, M., Hoff, G., Kim, C. H. & Saracco, P. (2016). *IEEE Trans. Nucl. Sci.* **63**, 1117–1146.

He, B. B. (2018). *Two-Dimensional X-ray Diffraction*, 2nd ed. New York: John Wiley & Sons.

Hemmers, O., Fisher, G., Glans, P., Hansen, D. L., Wang, H., Whitfield, S. B., Wehlitz, R., Levin, J. C., Sellin, I. A., Perera, R. C. C., Dias, E. W. B., Chakraborty, H. S., Deshmukh, P. C., Manson, S. T. & Lindle, D. W. (1997). *J. Phys. B At. Mol. Opt. Phys.* **30**, L727–L733.

Holbrook, C., Chakraborty, S., Ravindren, S., Boolchand, P., Goldstein, J. T. & Stutz, C. E. (2014). *J. Chem. Phys.* **140**, 144506.

Jakoncic, J., Di Michiel, M., Zhong, Z., Honkimaki, V., Jouanneau, Y. & Stojanoff, V. (2006). *J. Appl. Cryst.* **39**, 831–841.

Kahn, R., Fourme, R., Gadet, A., Janin, J., Dumas, C. & André, D. (1982). *J. Appl. Cryst.* **15**, 330–337.

Klein, O. & Nishina, Y. (1929). *Z. Phys.* **52**, 853–868.

Klug, H. P. & Alexander, L. E. (1974). *X-ray Diffraction Procedures For Polycrystalline and Amorphous Materials*, 2nd ed. Weinheim: Wiley-VCH.

Krogh-Moe, J. (1956). *Acta Cryst.* **9**, 951–953.

Li, H., Hackenschmied, P., Epelbaum, E. & Batentschuk, M. (2002). *Mater. Sci. Eng. B*, **94**, 32–39.

Manninen, S., Pitkänen, T., Koikkalainen, S. & Paakkari, T. (1984). *Int. J. Appl. Radiat. Isot.* **35**, 93–98.

Marcial, J., Saleh, M., Watson, D., Martin, S. W., Crawford, C. L. & McCloy, J. S. (2019). *J. Non-Cryst. Solids*, **506**, 58–67.

Meadowcroft, A. L., Bentley, C. D. & Stott, E. N. (2008). *Rev. Sci. Instrum.* **79**, 113102.

Meredith, C. C., Moberly, J. W. & Barlow, M. (1969). *J. Less-Common Met.* **18**, 423–425.

Paalman, H. H. & Pings, C. J. (1962). *Rev. Sci. Instrum.* **33**, 496–497.

Reibenspies, J. H. & Bhuvanesh, N. (2009). *Powder Diffr.* **24**, 56–58.

Rodriguez, M. A., Boyle, T. J., Yang, P. & Harris, D. L. (2008). *Powder Diffr.* **23**, 121–124.

Rowlands, J. A. (2002). *Phys. Med. Biol.* **47**, R123–R166.

Serimaa, R., Pitkänen, T., Vahvaselkä, S. & Paakkari, T. (1990). *J. Appl. Cryst.* **23**, 11–17.

Skinner, L. B., Benmore, C. J. & Parise, J. B. (2012). *Nucl. Instrum. Methods Phys. Res. A*, **662**, 61–70.

Soper, A. K. & Barney, E. R. (2011). *J. Appl. Cryst.* **44**, 714–726.

Strachan, D. M., Schaef, H. T., Schweiger, M. J., Simmons, K. L., Woodcock, L. J. & Krouse, M. K. (2003). *Powder Diffr.* **18**, 23–28.

Tisseur, D., Costin, M., Mathy, F. & Schumm, A. (2014). *AIP Conf. Proc.* **1581**, 1861–1867.

Trzhaskovskaya, M. B., Nefedov, V. I. & Yarzhemsky, V. G. (2001). *At. Data Nucl. Data Tables*, **77**, 97–159.

Trzhaskovskaya, M. B., Nefedov, V. I. & Yarzhemsky, V. G. (2002). *At. Data Nucl. Data Tables*, **82**, 257–311.

Waasmaier, D. & Kirfel, A. (1995). *Acta Cryst.* A**51**, 416–431.

Wright, A. C. (1994). *J. Non-Cryst. Solids*, **179**, 84–115.

Zaleski, J., Wu, G. & Coppens, P. (1998). *J. Appl. Cryst.* **31**, 302–304.

Zimina, A., Dardenne, K., Denecke, M. A., Doronkin, D. E., Huttel, E., Lichtenberg, H., Mangold, S., Pruessmann, T., Rothe, J., Spangenberg, T., Steininger, R., Vitova, T., Geckeis, H. & Grunwaldt, J.-D. (2017). *Rev. Sci. Instrum.* **88**, 113113.